Journal of Crystal Growth 460 (2017) 98–104

Contents lists available at ScienceDirect

Journal of Crystal Growth

journal homepage: www.elsevier.com/locate/jcrysgro

Precipitation of Cu and Ni in n- and p-type Czochralski-grown silicon characterized by photoluminescence imaging

Chang Sun*, Hieu T. Nguyen, Fiacre E. Rougieux, Daniel Macdonald

Research School of Engineering, The Australian National University, Canberra ACT 2601, Australia

ARTICLE INFO

Keywords:
A1. Characterisation
A1. Photoluminescence imaging
A1. Metal precipitates
A1. Point defects
A1. Doping
B2. Semiconducting silicon

ABSTRACT

Photoluminescence (PL) images and micro-PL maps were taken on Cu- or Ni-doped monocrystalline silicon wafers, to investigate the distribution of the metal precipitates. Several n-type and p-type wafers were used in which Cu or Ni were introduced in the starting melt of the ingots and precipitated during the ingot cooling (as opposed to surface contamination). The micro-PL mapping allowed investigation of the metal precipitates with a higher spatial resolution. Markedly different precipitation patterns were observed in n- and p-type samples: in both Cu- and Ni-doped n-type samples, circular central regions and edge regions were observed. In these regions, particles were distributed randomly and homogeneously. In the p-type Cu-doped and Ni-doped samples, by contrast, the precipitates occurred in lines along <110> orientations. The difference in the precipitation behaviour in n- and p-type samples is conjectured to be caused by different concentrations of self-interstitials and vacancies remaining in the crystal during the ingot cooling: there are more vacancies in the n-type ingots but more interstitials in the p-type ingots. The dopant effects on the intrinsic point defect concentrations in silicon crystals and possible precipitation mechanisms are discussed based on the findings in this work and the literature.

1. Introduction

Cu and Ni are two of the most common metallic impurities in silicon [1–3]. Due to their high diffusivities and solubilities, contamination can occur easily during the production and processing of wafers [1–3]. Cu and Ni mostly exist as precipitates in silicon at room temperature. The detrimental effects of the precipitates on the carrier lifetime of silicon materials as well as on the performance of solar cells are well recognized [1–4]. Band-like deep states have been detected in silicon wafers contaminated with Cu or Ni by applying deep-level transient spectroscopy (DLTS) [5–10].

The recombination-active areas due to the metal precipitates are visible in photoluminescence (PL) images [11]. In this work we characterise the Cu and Ni precipitates applying both PL imaging and micro-PL mapping to several n- and p-type Czochralski-grown (Cz) silicon wafers, in which deliberately-added Cu or Ni had precipitated during the ingot growth. In comparison with PL imaging, the micro-PL mapping allows more highly resolved inspection of the precipitates, because of the smaller pixel size, and also because the much higher injection level achieved during the measurement makes the carrier lifetime Auger limited, thus reducing the carrier diffusion [12]. Strikingly different distribution patterns of the particles were observed in n- and p-type samples. We propose that the different precipitation behaviours of the metals reveal different concentrations of vacancies and interstitials incorporated into the growing silicon crystal, which have significant effects on the precipitation behaviours of the metals. The dopant effects on the point defect concentrations during the ingot growth are then discussed based on the findings of this work, and the literature.

2. Experiments

2.1. Sample preparation

The samples used in this work were from six Czochralski (Cz) ingots specially grown by SiliConsultant [13]. The ingots were pulled from <100> seeds, with a 2 mm/min speed at the full diameter (around 25 mm, in the 23–31 mm range). For each doping type, one ingot was grown as a control ingot; one was intentionally doped with Cu and one with Ni. Samples at similar solidified fractions in the middle of the ingots were selected for this study. The samples were chemically etched to remove saw damage, and then passivated with Plasma-Enhanced Chemical Vapor Deposited (PECVD) SiN films. The boron (*p*-type) and phosphorus (*n*-type) doping levels $N_{A/D}$ of the samples were in the

* Corresponding author.
E-mail address: chang.sun@anu.edu.au (C. Sun).

http://dx.doi.org/10.1016/j.jcrysgro.2016.12.084
Received 22 June 2016; Received in revised form 22 November 2016; Accepted 20 December 2016
Available online 23 December 2016

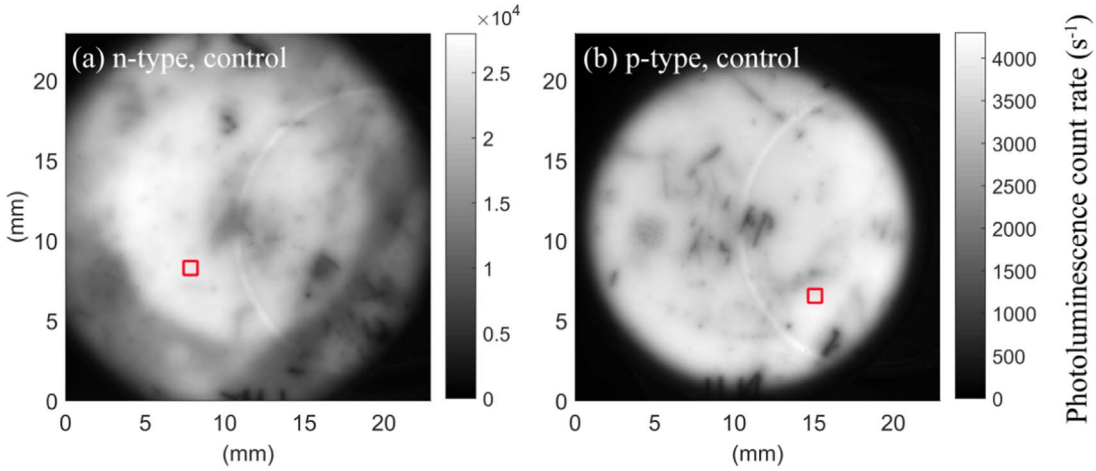

Fig. 1. Images of PL count rate (s^{-1}) of the (a) n-type and (b) p-type control samples. The red square illustrate the areas where the micro-PL maps were taken.

range of $(1.3 \pm 0.4)\times10^{16}$ cm^{-3}, determined with the dark conductance method [14]. The concentrations of Cu ([Cu]) in the Cu-doped samples were within $(2 \pm 0.4)\times10^{15}$ cm^{-3}, and the concentrations of Ni ([Ni]) in the Ni-doped samples were within $(1.2 \pm 0.2)\times10^{14}$ cm^{-3}, as estimated by applying the Scheil law, with the effective segregation coefficients of Cu and Ni taken as 8×10^{-4} [15,16], and 3.2×10^{-5} [15,17], respectively, combined with the known starting concentrations in the melt of [Cu] $=1.29\times10^{18}$ cm^{-3} and [Ni]$=1.68\times10^{18}$ cm^{-3}, respectively. The control samples were confirmed to be dislocation-free by conducting defect etching [18], after taking all the images and maps.

2.2. PL imaging and micro-PL mapping systems

The PL images were obtained using a LIS-R1 PL imaging system from BT imaging [19]. The pixel size of the PL images was 23 μm. The images were taken with a fixed photo flux of $(1.9 \pm 0.1)\times10^{18}$ cm^{-2} s^{-1}. The injection level was estimated to be in the range of 10^{15}–10^{16} cm^{-3}.

The micro-PL mapping system used in this study was a Horiba T64000 system equipped with a confocal microscope. The step size of the maps was 6 μm in both directions. For the central region of the n-type Cu-doped sample, two different excitation wavelengths, 525 nm and 795 nm were used for the incident laser beam to investigate the depth distribution of the particles. For other regions and samples, only the 795 nm excitation wavelength was used. The on-sample size of the 525 nm wavelength and the 795 nm wavelength was 1.2 μm and 1.8 μm in diameter, respectively. The on-sample average intensity was within 31.5 ± 1.5 mW for both excitation wavelengths. The order of magnitude of the injection level was estimated to be in the range of 10^{18}–10^{19} cm^{-3}. All the measurements were performed at room temperature.

3. Results

3.1. PL images

Fig. 1 shows the PL count rate images of the n- and p-type control samples. The bright rings which are non-concentric with the samples and appear in almost all of Figs. 1–3 are artefacts caused by luminescence reflected from the photo-conductance coil in the PL imager. The images show relatively uniform high-signal areas, although there are some surface scratches evident which are not related to the ingot growth. The PL images of the Cu-doped samples are shown in Fig. 2, and those of the Ni-doped samples are shown in Fig. 3. The red square or rectangle labels in Figs. 1–3 illustrate the areas where the micro-PL maps were taken. The dark crosses in Fig. 2(a) and the dark squares and the upright and horizontal straight lines in Figs. 2(b) and 3(b) are laser lines for locating specific regions. In the image of the n-type Cu-doped sample (2(a)), particles are not easily distinguished. A high-signal ring structure can be seen, dividing the sample into a central region and an edge region. Within each region, the PL signal is relatively uniform. The origin of the ring structure will be discussed in Section 4.4. In the n-type Ni-doped sample (Fig. 3(a)), particles are

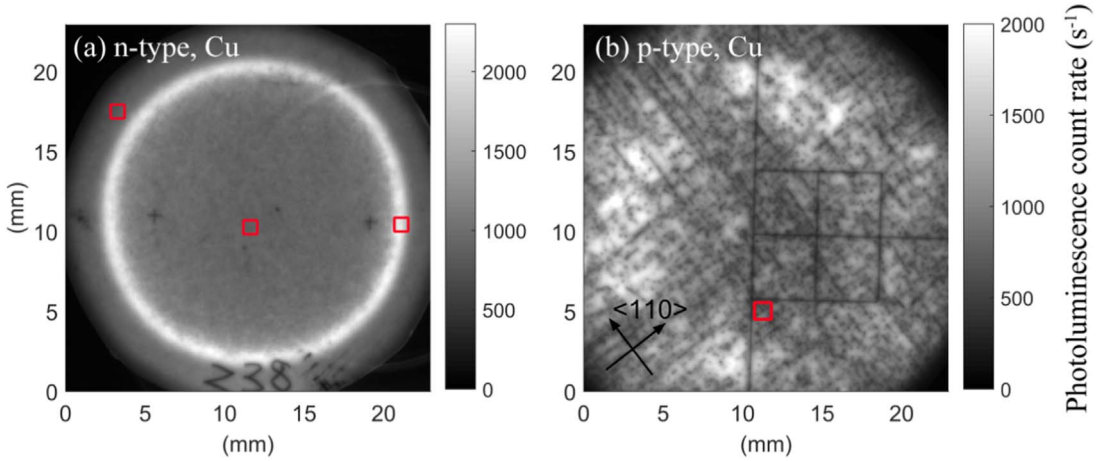

Fig. 2. Images of PL count rate (s^{-1}) of the (a) n-type and (b) p-type Cu-doped samples. The red square labels illustrate the areas where the micro-PL maps were taken. The dark crosses in (a) and the dark squares and the upright and horizontal straight lines in (b) are laser lines for locating specific regions. The orientations of the lined-up colonies of the particles in (b) were identified as the $<110>$ direction as indicated by the arrows.

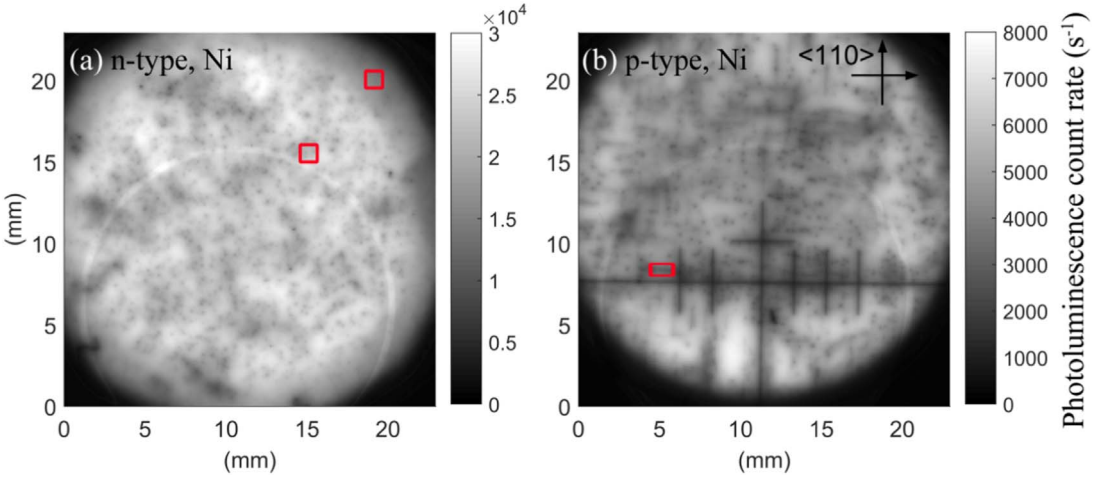

Fig. 3. Images of PL count rate (s^{-1}) of the (a) n-type and (b) p-type Ni-doped samples. The red square or rectangle labels illustrate the areas where the micro-PL maps were taken. The upright and horizontal straight lines in (b) are laser lines for locating specific regions. The orientations of the lined-up colonies of the particles in (b) were identified as the < 110 > direction as indicated by the arrows.

more clearly visible, possibly due to the sparser precipitate particles in comparison with the n-type Cu-doped sample, as [Ni] is much lower than [Cu] ([Ni] =1.2×10^{14} cm^{-3} whilst [Cu] =2.0×10^{15} cm^{-3}). There is slightly lower signal at the edge, and we refer to this circular lower-signal region as the edge region. The rest is referred to as the central region. We can see that within each region, the particles distribute randomly and homogeneously. By contrast, in both the p-type Cu-doped sample (Fig. 2(b)) and Ni-doped sample (Fig. 3(b)), lined-up colonies of particles in two perpendicular orientations can be seen. Based on the known orientation of the seed crystal and the resulting wafer surface, the orientation of the lined-up particles was identified as the < 110 > direction (as indicated in Figs. 2(b) and 3(b)), by comparison with natural cleave lines obtained by cleaving several samples from the p-type Cu-doped ingot, and several samples from the p-type Ni-doped ingot, in which we observed similar lined-up colonies of particles.

3.2. Micro-PL maps

Micro-PL maps of the areas labelled in Figs. 1–3 were then taken. Almost no particles were seen in the maps of the control samples, as shown by Fig. 4. The micro-PL maps of areas in the central region, the ring region and the edge region of the n-type Cu-doped sample are shown in Figs. 5 and 6. Particles are visible in the micro-PL maps in every region. In the central region (5(a)), it can be observed that some of the particles have higher contrast than the others, while in the edge region (6(b)), most of the particles have lower contrast, but appear in a higher density. There is a much lower density of particles in the ring region compared with other regions. The left of Fig. 6(a) is close to the central region, and the right is close to the edge region, as indicated by the square label in Fig. 2(a). From the left to the right, fewer higher-contrast particles but more lower-contrast particles can be seen, indicating a transition of the particle type. The different types of particles in the central and edge region are also observed in the n-type Ni-doped sample, as shown in Fig. 7. Fig. 7 also reveals that the higher-contrast particles have larger sizes than the lower-contrast ones.

Fig. 8 shows the micro-PL map of an area on the p-type Cu-doped sample, and Fig. 9 shows the micro-PL map of an area on the p-type Ni-doped sample. Similar features with the PL images are observed in the maps, but with a higher spatial resolution. In addition, it can be seen that the lines of the particles are not perfectly straight, but heavily jogged and discontinuous.

The detection depth of the micro-PL can be roughly estimated based on the larger of the absorption length and the carrier diffusion length, with the latter assumed to be Auger-limited. This gives an approximate detection depth of 40 μm. The number of metal atoms contained in each particle can then be estimated based on the volume density of particles observed in the micro-PL maps (using the 795 nm laser). Assuming that the precipitates are Cu_3Si and $NiSi_2$ [3,20], the size of the particles can be then estimated. The sizes (in one dimension) of the Cu_3Si and $NiSi_2$ particles are thus estimated to be in the 0.1–1 μm range, and the 0.1–0.5 μm range, respectively, which are in

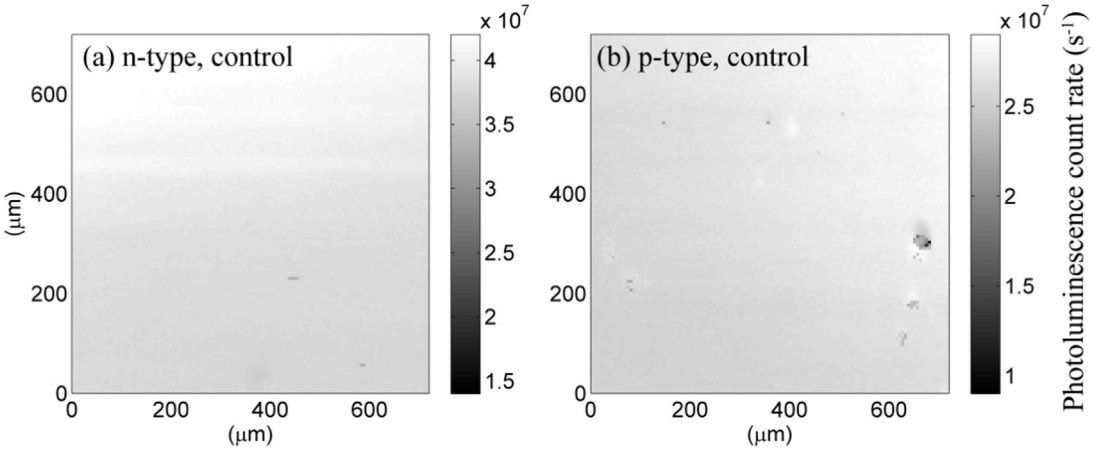

Fig. 4. Micro-PL maps of a 720 μm×720 μm area on the (a) n-type and (b) p-type control samples.

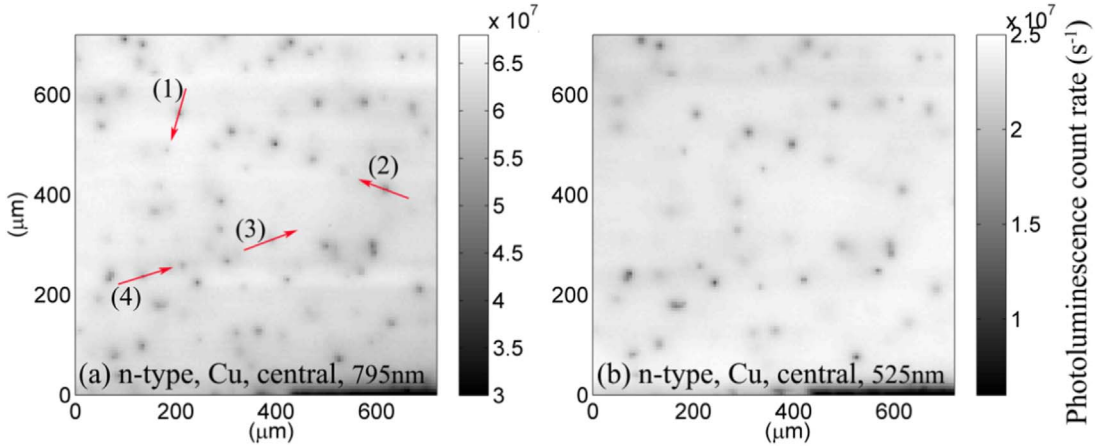

Fig. 5. Micro-PL maps of a 720 μm×720 μm area in the central region of the n-type Cu-doped sample. To investigate the depth distribution of the particles, two excitation wavelengths (a) 795 nm, and (b) 525 nm were used to map the same area. The arrows in (a) illustrate where line scans of the PL signal were extracted (as presented in Fig. 10 and discussed in Section 3.3).

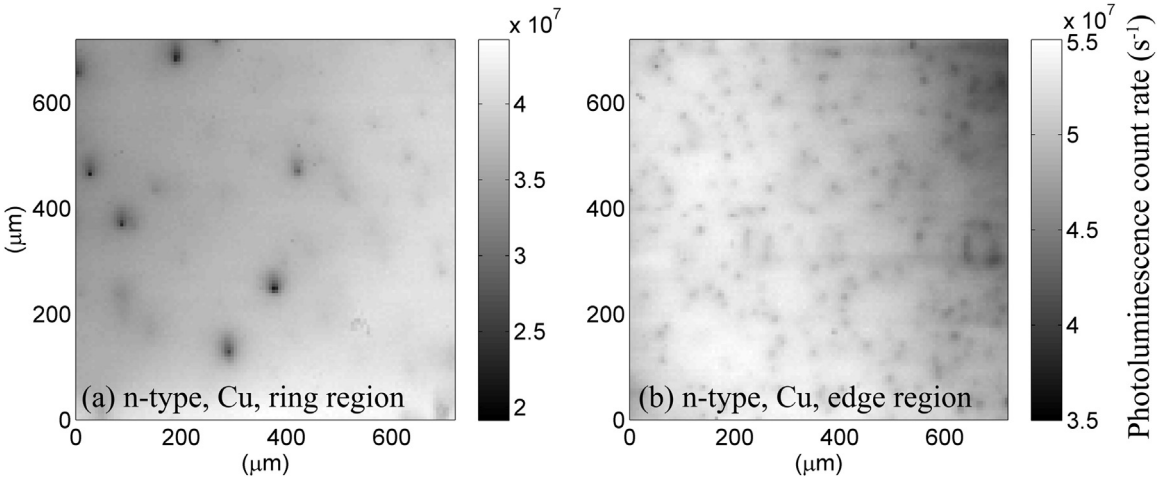

Fig. 6. Micro-PL maps of a 720 μm×720 μm area on the n-type Cu-doped sample in the (a) ring region and (b) edge region.

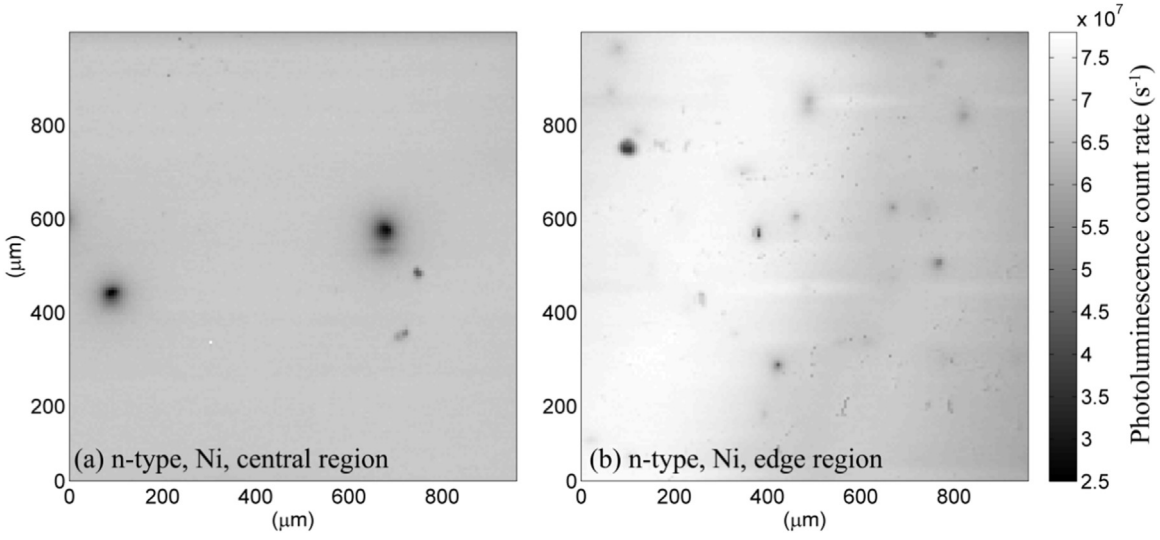

Fig. 7. Micro-PL maps of a 960 μm×960 μm area on the n-type Ni-doped sample in the (a) central region and (b) edge region.

agreement with the literature [3,21].

3.3. Micro-PL maps with different excitation wavelengths

To investigate the depth distribution of the particles, two different excitation wavelengths 795 nm and 525 nm were used to map the same area in the central region of the n-type Cu-doped sample, and the maps are shown in Fig. 5. At room temperature, the absorption depths of the 525 nm and 795 nm wavelengths are 1.16 μm and 11.56 μm, respectively [22]. As a result, a particle located deeply underneath the surface

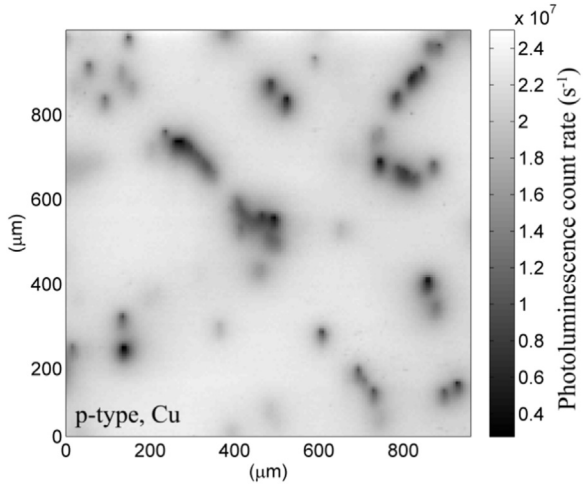

Fig. 8. Micro-PL map of a 960 μm×960 μm area on the p-type Cu-doped sample.

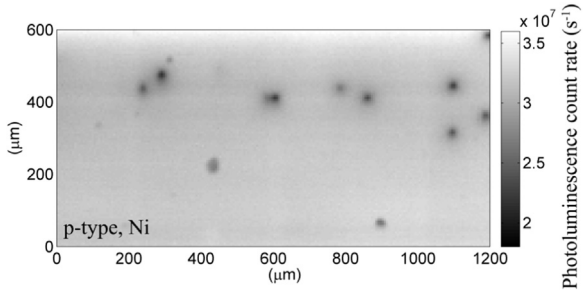

Fig. 9. Micro-PL map of a 600 μm×1200 μm area on the p-type Ni-doped sample.

detected by the 795 nm wavelength should display a higher contrast than that detected by the 525 nm wavelength [23]. To compare the results more directly, line scans of the signal on several particles were extracted. The lines are labelled as arrows in Fig. 6(a), and the results are shown in Fig. 10, where the signal was locally normalized. The two particles shown in Fig. 10(1) and (2) have similar contrast for both wavelengths, thus they should be on or close to the surface of the wafer. By comparison, the particles in (3) and (4) show an obviously higher contrast when detected by the 795 nm wavelength, indicating they are deeper in the bulk. This result indicates that the particles are not surface precipitates but rather precipitated throughout the thickness of the wafers, as expected when formed during ingot cooling.

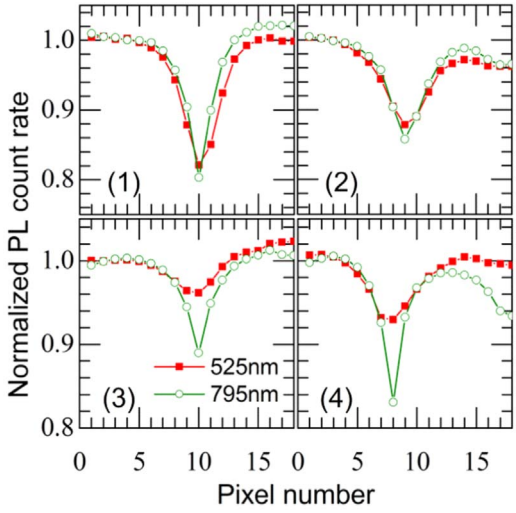

Fig. 10. Line scans of PL signal on several particles detected by the 525 nm and 795 nm wavelengths in the central region of the n-type Cu-doped sample. The numbers (1)~(4) of the figures correspond to the labels in Fig. 5(a). The legend in (3) holds for all four figures.

4. Discussion

4.1. Excluding the 'charged Cu precipitates' model as an explanation of the observations

The difference between the precipitation behaviours of Cu in n- and p-type silicon (n-Si and p-Si) at room temperature has been reported before [24–26]. Some authors have attributed the difference to the differently charged Cu precipitates in n-Si and p-Si: The Cu precipitates have an electro-neutrality level at about E_c–0.2 eV thus are positively charged at room temperature in p-Si. The existing precipitates will therefore repel the diffusing Cu_i^+, hindering further precipitation. This Coulomb repulsion does not exist in n-Si so the precipitation will not be hindered. However, this model cannot serve as a satisfactory explanation for the observations in this work. At about 500 °C, silicon with the doping levels of the samples in this work is effectively intrinsic. As calculated based on Ref. [3], the solubilities of Cu and Ni at 500 °C are 1.1×10^{14} cm^{-3} and 1.4×10^{13} cm^{-3}, respectively. For both Cu- and Ni-doped samples, the concentration of the metal is >10 times higher than the solubility, so the metals are highly super saturated. Being fast diffusers, Cu and Ni should have precipitated almost quantitatively above 500 °C during the relatively slow cooling down of the Cz ingots [3]. In this temperature range, silicon is intrinsic, and the Fermi level is at the mid-gap so the charge state of the precipitates is the same in both types of silicon. Therefore the different distributions of precipitates in n- and p-Si observed in this work are not likely to be caused by different charge states of the precipitates.

4.2. The effects of interstitials and vacancies on the precipitation of Cu and Ni

When Cu nucleates and precipitates in Si, the stress due to the volume expansion can be released by the emission of self-interstitials [3,8]. It has been reported that in a vacancy-rich zone in silicon, Cu preferably nucleates and precipitates near vacancies and voids which can absorb these emitted interstitials [27,28]. As a result, in a vacancy-rich region, the precipitates distribute randomly and homogeneously following the distribution of vacancies and voids [27,28], which conforms with our observations in the n-type Cu-doped sample.

However, in interstitial-rich silicon, the precipitates tend to form dislocation-related colonies [29]: during the precipitation of Cu, many interstitials are emitted, and the supersaturated interstitials will aggregate into dislocations, due to the absence of vacancy-related defects for them to recombine with. A climbing interstitial-type dislocation absorbs interstitials and emits vacancies [30], favouring the nucleation and precipitation of Cu, which in turn emits more interstitials, pushing the dislocations to climb [30,31]. As a result, the precipitates align along the climbing dislocations. This mechanism of repeated precipitation on climbing dislocations was studied in detail in Refs. [32–36]. Note that this is different from the Cu decoration of slip lines in silicon. In the decoration of slip lines, the dislocations exist before Cu precipitates, so the decoration will occur along straight lines [37]. While in the repeated precipitation on dislocations, the precipitation of Cu and the climbing of dislocations occur simultaneously in originally dislocation-free silicon. This results in heavily jogged dislocations and imperfect lines of precipitates [29,30,32,33,36]. This is consistent with our observations in the p-type Cu-doped sample, as revealed by Fig. 9. Colonies of Cu precipitates due to climbing dislocations with Burger's vectors of b=a/2 < 110 > and b=a < 100 > were reported previously [32], in agreement with the preferred precipitation orientation of < 110 > identified in this work.

For Ni, the lattice parameter of Ni precipitates matches better with the silicon matrix compared with Cu [3]. At 450 °C, it fits well with the

matrix; at higher temperatures it is larger while at lower temperatures it is smaller, due to the different temperature-dependence of the lattice [3]. If Ni precipitates form at 500–600 °C, interstitials are also emitted. Thus the effects of interstitials and vacancies on the precipitation of Ni should be similar to Cu. Ni precipitation assisted by voids has been reported in Ref. [38]. In addition, the atomic volume change associated with copper precipitation as Cu_3Si, and nickel precipitation as $NiSi_2$ are 50% and 0.4%, respectively [5]. Thus the less pronounced structures (including the bright ring structure in n-Si and lined-up colonies in p-Si) observed in the Ni-doped samples could either be caused by the much lower [Ni] than [Cu], or the lower sensitivity of precipitation behaviours of Ni to the intrinsic point defect non-equilibrium, or both."

Therefore the observations in the n- and p-type samples in this work imply that there could be more vacancies in the n-type ingots but more interstitials in the p-type ingots.

4.3. Grown-in intrinsic point defects and the effects of dopants

Based on Voronkov's theory [39], the type of intrinsic point defect which is dominant in a crystal depends on the ratio of the growth rate V and the temperature gradient G at the solid/liquid interface. When $V/G > (V/G)_{critical}$, vacancies are grown in; when $V/G < (V/G)_{critical}$, interstitials are grown in. In principle the ingots grown for this study are grown in vacancy-rich mode with a pulling speed of 2 mm/min. However, the p-type ingots could have been switched to interstitial-rich mode due to the dopant effects. The effects of the dopants B and P on the incorporation of the intrinsic point defects have been reported in several previous studies [40–45]:

a) Murarka *et al.* investigated the oxidation induced stacking faults (OiSF) in P-doped n-type and B-doped p-type Cz ingots with resistivites in the range of 0.6–40 Ω cm and found that, for n- and p-type ingots with similar resistivities, the concentration of OiSF is always at least one order of magnitude higher in n-type ingots than p-type ingots [40]. It was not understood at that time. As OiSF formation is related to the oxide particles formed in the vacancy-rich zone [46,47], their results could imply that there are more vacancies in the n-type ingots than p-type ingots.
b) Kock *et al.* explained the higher concentration of vacancies ([V]) in n-Si and higher concentration of interstitials ([I]) in p-Si by the pairing of the intrinsic defects with the dopants [41]. At intrinsic temperature, interstitials are negatively charged thus pair with P^+, whilst vacancies are positively charged and pair with B^-, resulting in higher [V] in P-doped n-Si but higher [I] in B-doped p-Si.
c) Dornberger *et al.* investigated the effects of B on the diameter of the OiSF ring, and showed that a certain [B] could shift the ring towards the wafer center (transition from vacancy-mode to interstitial-mode) [42]. They suspected the reason to be the size and chemical effects of B atoms.
d) Voronkov *et al.* explained that the value of $(V/G)_{critical}$ could be changed by the dopants, caused by Fermi level effects, impurity-induced strain or intrinsic point defect trapping by the impurities [43–45]. We can now exclude the Fermi level effects as the intrinsic point defects should be incorporated at intrinsic temperatures, when the Fermi level is at the mid-gap in both types of silicon.

Although there are various mechanisms proposed in the literature, these studies showed that a certain amount of phosphorus favours the presence of vacancies in a crystal, while a certain amount of boron favours the presence of interstitials, supporting the proposed model of precipitate formation in this study.

In addition, in comparison with the previous studies, it seems that it takes much smaller amount of dopants to shift the balance to an interstitial-rich crystal in this study. This could be possibly explained by the much smaller diameter of the ingots. The diameter of the ingots has a significant effect on G [42]. For ingots with such small diameters (around 25 mm) as in this work, G is much larger than ingots with larger diameters [42]. As a result, V/G could be very low yet above the critical value, making it much easier to totally switch the ingot growth to interstitial-mode.

4.4. The structure in n-Si: related to the bands in vacancy-rich region

The vacancy-rich zone consists of three bands with different concentrations of vacancies and voids [46–48], which is the likely reason why different regions were observed in the n-type samples. The three bands are [46–48]:

a) H-band. It is in the central region and has the highest starting [V]. The vacancies in this region tend to agglomerate into voids. Thus the particles with higher contrast, larger sizes and a lower density could be precipitates on the voids, while the particles with lower contrast, smaller sizes and a higher density could be precipitates on vacancies.
b) P-band. It is outside the H-band. In this region, vacancies react with oxygen and form oxide particles. The remaining [V] is the lowest among the three bands. This could be the ring region where the metals tend to diffuse to other regions rather than nucleate and precipitate within the band.
c) L-band. It is outside the P-band, and has the lowest starting [V]. In this band vacancies neither form voids nor react with oxygen, and the remaining [V] is similar with the H-band. This could be the edge region in the n-type samples, where the particles are mostly precipitates on isolated vacancies.

5. Conclusions

Both PL imaging and micro-PL mapping were applied to characterizing the Cu and Ni precipitates in n- and p-type Cz silicon wafers. The micro-PL mapping allowed greater spatial resolution of the metal precipitates, and by applying different excitation wavelengths, the particles were found to be distributed throughout the thickness of the wafers.

Markedly different precipitation patterns were observed in n- and p-type samples. In the n-type Cu-doped sample, a particle-lean ring structure was observed, dividing the sample into a central region and an edge region. Within each region, particles are distributed randomly and homogeneously. However, in the p-type Cu-doped sample, the precipitates occurred in lines along <110> orientations. For each type, the Ni-doped sample showed similar features to the Cu-doped sample. The difference in the precipitation behaviours in n- and p-type samples is conjectured to be caused by different concentrations of interstitials and vacancies remaining in the crystal during the ingot cooling: there are more vacancies in the n-type ingots but more interstitials in the p-type ingots. The metals preferably precipitate on defects to lower the energy barrier: in a vacancy-rich zone, they precipitate near vacancies and voids which absorb interstitials; while in an interstitial-rich zone, the climbing of interstitial-type dislocations and repeated nucleation of the metals occur simultaneously. In this work the orientations <110> along which the metals nucleate were identified for both Cu and Ni. Different intrinsic point defect concentrations in n- and p-type silicon ingots have been reported in several previous studies, and the authors have attributed it to the interactions between the intrinsic point defects and the dopants. Regardless of the physical cause, this observation has implications for high purity silicon ingots. Indeed, the contrast in intrinsic point defect concentrations between n- and p-type silicon is likely to lead to distinct types of growth- and process-induced defects in such materials, and hence different impacts on minority carrier lifetimes and devices.

Acknowledgements

This work has been supported through the Australian Renewable Energy Agency (ARENA) projects 1-GER010 and RND009, and the Australian Centre for Advanced Photovoltaics. Support from the Australian Research Council (ARC) DECRA and Future Fellowships programs are also acknowledged. The authors are indebted to Professor Hoe Tan for providing access to the spectroscopic equipment.

References

[1] E.R. Weber, Transition metals in silicon, Appl. Phys. A 30 (1983) 1–22.
[2] A. Istratov, E. Weber, Electrical properties and recombination activity of copper nickel cobalt in silicon, Appl. Phys. A 66 (1998) 123–136.
[3] K. Graff, Metal Impurities in Silicon-Device Fabrication, Springer, Berlin, 2000.
[4] G. Coletti, P.C. Bronsveld, G. Hahn, W. Warta, D. Macdonald, B. Ceccaroli, K. Wambach, N. Le Quang, J.M. Fernandez, Impact of metal contamination in silicon solar cells, Adv. Funct. Mater. 21 (2011) 879–890.
[5] M. Seibt, H. Hedemann, A. Istratov, F. Riedel, A. Sattler, W. Schröter, Structural and electrical properties of metal silicide precipitates in silicon, Physica Status Solidi(a) 171 (1999) 301–310.
[6] F. Riedel, W. Schröter, Electrical and structural properties of nanoscale NiSi 2 precipitates in silicon, Phys. Rev. B 62 (2000) 7150.
[7] M. Kittler, J. Lärz, W. Seifert, M. Seibt, W. Schröter, Recombination properties of structurally well defined NiSi2 precipitates in silicon, Appl. Phys. Lett. 58 (1991) 911–913.
[8] M. Seibt, M. Griess, A. Istratov, H. Hedemann, A. Sattler, W. Schröter, Formation and properties of copper silicide precipitates in silicon, Physica Status Solidi (A) 166 (1998) 171–182.
[9] M. Trushin, O. Vyvenko, Electrical levels of nanoscale NiSi2 precipitates in silicon band gap, Physica Status Solidi (C) 4 (2007) 3056–3060.
[10] M. Trushin, O. Vyvenko, M. Seibt, Impact of NiSi2 precipitates electronic structure on the minority carrier lifetime in n-and p-type silicon, Solid State Phenom. 131 (2008) 155–160.
[11] P. Gundel, M.C. Schubert, W. Kwapil, J. Schön, M. Reiche, H. Savin, M. Yli-Koski, J.A. Sans, G. Martinez-Criado, W. Seifert, Micro-photoluminescence spectroscopy on metal precipitates in silicon, Physica Status Solidi (RRL)-Rapid Res. Lett. 3 (2009) 230–232.
[12] P. Gundel, F.D. Heinz, M.C. Schubert, J.A. Giesecke, W. Warta, Quantitative carrier lifetime measurement with micron resolution, J. Appl. Phys. 108 (2010) 033705.
[13] ⟨http://www.siliconsultant.com/⟩. 22/06/2016.
[14] R.A. Sinton, A. Cuevas, Contactless determination of current–voltage characteristics and minority-carrier lifetimes in semiconductors from quasi-steady-state photoconductance data, Appl. Phys. Lett. 69 (1996) 2510–2512.
[15] J.R. Davis Jr, A. Rohatgi, R. Hopkins, P. Blais, P. Rai-Choudhury, J. McCormick, H. Mollenkopf, Impurities in silicon solar cells, electron devices, IEEE Trans. 27 (1980) 677–687.
[16] R. Hopkins, A. Rohatgi, Impurity effects in silicon for high efficiency solar cells, J. Cryst. Growth 75 (1986) 67–79.
[17] R. Hopkins, R. Seidensticker, J. Davis, P. Rai-Choudhury, P. Blais, J. McCormick, Crystal growth considerations in the use of "solar grade" silicon, J. Cryst. Growth 42 (1977) 493–498.
[18] Y. Kashiwagi, R. Shimokawa, M. Yamanaka, Highly sensitive etchants for delineation of defects in single-and polycrystalline silicon materials, J. Electrochem. Soc. 143 (1996) 4079–4087.
[19] T. Trupke, R. Bardos, M. Schubert, W. Warta, Photoluminescence imaging of silicon wafers, Appl. Phys. Lett. 89 (2006) 044107.
[20] J.K. Solberg, The crystal structure of η-Cu3Si precipitates in silicon, Acta Crystallogr. Sect. A: Cryst. Phys., Diffr., Theor. Gen. Crystallogr. 34 (1978) 684–698.
[21] M. Seibt, K. Graff, Characterization of haze-forming precipitates in silicon, J. Appl. Phys. 63 (1988) 4444–4450.
[22] C. Schinke, K. Bothe, P.C. Peest, J. Schmidt, R. Brendel, Uncertainty of the coefficient of band-to-band absorption of crystalline silicon at near-infrared wavelengths, Appl. Phys. Lett. 104 (2014) 081915.
[23] H.T. Nguyen, S.P. Phang, J. Wong-Leung, D. Macdonald, Photoluminescence excitation spectroscopy of diffused layers on crystalline silicon wafers, IEEE, J. Photovolt. 6 (2016) 746–753.
[24] A. Istratov, H. Hedemann, M. Seibt, O. Vyvenko, W. Schröter, T. Heiser, C. Flink, H. Hieslmair, E. Weber, Electrical and recombination properties of copper-silicide precipitates in silicon, J. Electrochem. Soc. 145 (1998) 3889–3898.
[25] R. Sachdeva, A. Istratov, E. Weber, Recombination activity of copper in silicon, Appl. Phys. Lett. 79 (2001) 2937–2939.
[26] A.A. Istratov, E.R. Weber, Physics of copper in silicon, J. Electrochem. Soc. 149 (2002) G21–G30.
[27] Z. Xi, J. Chen, D. Yang, A. Lawerenz, H. Moeller, Copper precipitation in large-diameter Czochralski silicon, J. Appl. Phys. 97 (2005) 094909.
[28] Y. Hu, H. Schøn, L. Arnberg, Characterization of defect patterns in Cz silicon slabs by carrier density imaging, J. Cryst. Growth 368 (2013) 6–10.
[29] W. Wang, D. Yang, X. Ma, D. Que, Effect of silicon interstitials on Cu precipitation in n-type Czochralski silicon, J. Appl. Phys. 103 (2008) 3534.
[30] G. Das, Precipitation of copper in silicon, J. Appl. Phys. 44 (1973) 4459–4467.
[31] W.K. Tice, T.Y. Tan, Nucleation of CuSi precipitate colonies in oxygen-rich silicon, Appl. Phys. Lett. 28 (1976) 564.
[32] E. Nes, J. Washburn, Precipitation in high-purity silicon single crystals, J. Appl. Phys. 42 (1971) 3562–3574.
[33] E. Nes, J. Washburn, Precipitate colonies in silicon, J. Appl. Phys. 43 (1972) 2005–2006.
[34] E. Nes, J. Solberg, In situ transmission electron microscope investigation of the annealing of copper precipitate colonies in silicon, J. Appl. Phys. 44 (1973) 486–487.
[35] E. Nes, The mechanism of repeated precipitation on dislocations, Acta Metall. 22 (1974) 81–87.
[36] J. Solberg, E. Nes, On the micromechanisms of repeated precipitation on edge dislocations, J. Mater. Sci. 13 (1978) 2233–2240.
[37] W. Dash, Copper precipitation on dislocations in silicon, J. Appl. Phys. 27 (1956) 1193–1195.
[38] Z. Xi, D. Yang, J. Chen, D. Que, H. Moeller, Nickel precipitation in large-diameter Czochralski silicon, Physica B: Condens. Matter 344 (2004) 407–412.
[39] V. Voronkov, The mechanism of swirl defects formation in silicon, J. Cryst. Growth 59 (1982) 625–643.
[40] S. Murarka, G. Quintana, Oxidation induced stacking faults in n-and p-type (100) silicon, J. Appl. Phys. 48 (1977) 46–51.
[41] A. De Kock, W. Van de Wijgert, The effect of doping on the formation of swirl defects in dislocation-free czochralski-grown silicon crystals, J. Cryst. Growth 49 (1980) 718–734.
[42] E. Dornberger, D. Gräf, M. Suhren, U. Lambert, P. Wagner, F. Dupret, W. von Ammon, Influence of boron concentration on the oxidation-induced stacking fault ring in Czochralski silicon crystals, J. Cryst. Growth 180 (1997) 343–352.
[43] V. Voronkov, R. Falster, Dopant effect on point defect incorporation into growing silicon crystal, J. Appl. Phys. 87 (2000) 4126–4129.
[44] V. Voronkov, R. Falster, Effect of doping on point defect incorporation during silicon growth, Microelectron. Eng. 56 (2001) 165–168.
[45] V. Voronkov, R. Falster, Intrinsic point defects and impurities in silicon crystal growth, J. Electrochem. Soc. 149 (2002) G167–G174.
[46] Y. Hu, Characterization of defects in n-type CZ silicon for solar cells (Ph.D. dissertation)Nor. Univ. Sci. Technol. (2012).
[47] R. Falster, V. Voronkov, F. Quast, On the properties of the intrinsic point defects in silicon: a perspective from crystal growth and wafer processing, Physica Status Solidi B Basic Res. 222 (2000) 219–244.
[48] V. Voronkov, Grown-in defects in silicon produced by agglomeration of vacancies and self-interstitials, J. Cryst. Growth 310 (2008) 1307–1314.